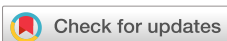


RESEARCH ARTICLE | MARCH 01 2023

Imaging x-ray spectrometer at the high energy density instrument of the European x-ray free electron laser

X. Pan ; M. Šmíd; R. Štefaníková; ... et. al



Rev Sci Instrum 94, 033501 (2023)
<https://doi.org/10.1063/5.0133639>



View
Online



Export
Citation

CrossMark

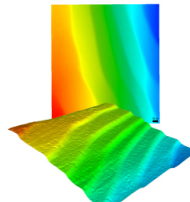
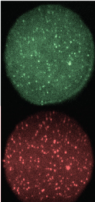
Articles You May Be Interested In

Research and analysis on the landslide characteristics of Xigeda soil slope

AIP Conference Proceedings (March 2018)

Status of the HERA-B experiment

AIP Conference Proceedings (February 1999)

 MAD CITY LABS INC. www.madcitylabs.com	Nanopositioning Systems 	Modular Motion Control 	AFM and NSOM Instruments 	Single Molecule Microscopes 
---	--	---	---	--

Imaging x-ray spectrometer at the high energy density instrument of the European x-ray free electron laser

Cite as: Rev. Sci. Instrum. 94, 033501 (2023); doi: 10.1063/5.0133639

Submitted: 4 November 2022 • Accepted: 3 February 2023 •

Published Online: 1 March 2023



View Online



Export Citation



CrossMark

X. Pan,^{1,2,a} M. Šmíd,¹ R. Štefaníková,^{1,2} F. Donat,¹ C. Baehtz,¹ T. Burian,³ V. Cerantola,⁴ L. Gaus,¹ O. S. Humphries,⁴ V. Hajkova,³ L. Juha,³ M. Krupka,³ M. Kozlová,^{1,3} Z. Konopkova,⁴ T. R. Preston,⁴ L. Wollenweber,⁴ U. Zastrau,⁴ and K. Falk^{1,2,3}

AFFILIATIONS

¹ Helmholtz-Zentrum Dresden-Rossendorf, 01328 Dresden, Germany

² Technische Universität Dresden, 01069 Dresden, Germany

³ Institute of Physics of the ASCR, 18221 Prague, Czech Republic

⁴ European XFEL, Holzkoppel 4, 22869 Schenefeld, Germany

^a Author to whom correspondence should be addressed: panxy@hzdr.de

ABSTRACT

A multipurpose imaging x-ray crystal spectrometer is developed for the high energy density instrument of the European X-ray Free Electron Laser. The spectrometer is designed to measure x rays in the energy range of 4–10 keV, providing high-resolution, spatially resolved spectral measurements. A toroidally bent germanium (Ge) crystal is used, allowing x-ray diffraction from the crystal to image along a one-dimensional spatial profile while spectrally resolving along the other. A detailed geometrical analysis is performed to determine the curvature of the crystal. The theoretical performance of the spectrometer in various configurations is calculated by ray-tracing simulations. The key properties of the spectrometer, including the spectral and spatial resolution, are demonstrated experimentally on different platforms. Experimental results prove that this Ge spectrometer is a powerful tool for spatially resolved measurements of x-ray emission, scattering, or absorption spectra in high energy density physics.

© 2023 Author(s). All article content, except where otherwise noted, is licensed under a Creative Commons Attribution (CC BY) license (<http://creativecommons.org/licenses/by/4.0/>). <https://doi.org/10.1063/5.0133639>

I. INTRODUCTION

In high energy density physics experiments, dense plasmas or warm dense matter (WDM) with large, one-dimensional gradients in the temperature, density, and ionization state can be created by intense laser irradiation. Measurements of these plasma parameters are essential to model the equation of state (EOS) of astrophysically relevant matter. X-ray Thomson scattering (XRTS) has been proven to be a powerful technique for diagnosing the internal conditions of dense plasmas or WDM.^{1–6}

In the XRTS technique, the probing x rays are scattered by single electrons or collective electron waves (known as plasmons) in the target plasma, then the spectral shape of the probing x rays is changed and encoded with the physical information about the plasma.⁷ XRTS measurements are usually challenging due to

the small scattering cross-section ($\sim 10^{-24} \text{ cm}^{-2}$); thus, a highly efficient spectrometer is necessary for this application.⁵ Highly ordered pyrolytic graphite (HOPG) or highly annealed pyrolytic graphite (HAPG) crystals have been extensively employed in the XRTS experiments due to the highly integrated reflectivity in a broad energy range.^{1–4,8} However, the mosaic graphite structure prevents HOPG/HAPG crystals from delivering a useful spatial resolution.⁹ Consequently, the scattered spectrum can be a superposition of scattered signals from a range of plasma conditions for the spatially inhomogeneous plasmas, making the deduction of the plasma conditions more challenging.⁸ In addition, the spectral resolution of the mosaic crystal spectrometers is usually low compared to the perfect crystals.^{9–11} A spectrometer with spatial resolution as well as good spectral resolution is beneficial to the XRTS experiments.

To diagnose inhomogeneous plasmas, the development of the spatially resolving x-ray spectrometer, also known as the imaging x-ray spectrometer, is needed. The imaging x-ray Thomson spectrometer (IXTS) has been developed for Trident and Omega laser facilities,^{12,13} Z-machine,¹⁴ and Matter in Extreme Conditions (MECs) end station of the Linac Coherent Light Source (LCLS).¹⁵ These spectrometers use a toroidally or spherically curved germanium (Ge) crystal that allows for imaging in one spatial dimension while spectrally resolving in the other. Based on the measured x-ray energy and specific geometrical requirements, different diffraction planes of the Ge crystal are employed.^{12–15} The nearly perfect Ge crystal is chosen due to its relatively high integrated reflectivity compared to other often used perfect crystals (e.g., silicon, quartz crystals),¹⁴ even though still lower than that of mosaic crystals. With the use of toroidal Ge crystals, 48 μm spatial resolution within a large field of view (>3 mm) combined with the spectral resolution of 4 eV at 4.75 keV can be achieved.^{12,13} By using these instruments, plasma parameters can be extracted along the spatial profile for the study of EOS and transport properties in WDM or dense plasmas, radiative shocks, and other potential applications in high energy density experiments.

In this article, we present the development of an imaging x-ray spectrometer for the High Energy Density (HED) instrument¹⁶ of the European X-ray Free Electron Laser (XFEL). There are several HAPG crystal spectrometers already fielded at the HED instrument of European XFEL,¹⁷ providing the spectrally resolved measurements for x-rays scattering or emission from the high energy density matter. These HAPG spectrometers offer resolving powers of ~ 1000 by using a 50 mm radius of curvature crystal, and ≤ 2800 when using an 80 mm radius of curvature, as well as high efficiency ($\sim 10^{-5}$ at 8.05 keV).¹⁷ Thus, to extend the ability of the spectroscopic diagnosis at the HED instrument, an imaging x-ray spectrometer with a focusing geometry similar to the IXTS at the Trident and Omega laser facilities^{12,13} is proposed. This spectrometer is a complementary addition to the existing spectrometers at the HED instrument. By distinguishing from the previously developed IXTS,^{12–14} this new imaging spectrometer is designed to measure x rays in a broad energy range rather than only measuring a narrow range around a fixed central energy. Therefore, this spectrometer can be used for the study of the high energy density states of different materials.

Detailed design considerations, including the geometrical analysis, are presented in the article. The performance of the spectrometer is estimated for various configurations by ray-tracing simulations. Several typical configurations are experimentally demonstrated and evaluated by measuring the characteristic radiation of a microfocus x-ray source and the self-emission spectra of the Cu plasma heated by the XFEL beam.

II. SPECTROMETER DESIGN

A. Basic requirements

The design of the imaging x-ray spectrometer for the HED instrument of the European XFEL has to meet several requirements. As discussed in Sec. I, high spatial- and spectral-resolution properties are desired to diagnose HED plasmas. The design goals for the spectrometer are 25 μm spatial resolution—dependent on accurate alignment—and < 5 eV spectral resolution at 10 keV ($E/\delta E > 2000$).

Furthermore, the spectrometer must be able to measure x rays in a broad energy range to study the extreme conditions of various materials. The energy range of 4–10 keV is desired because the photon energies employed in high energy density experiments typically range from 4 to 10 keV, and the characteristic K-shell emission from metal targets such as Ti (~4.5 keV) or Cu (~8.0 keV) are commonly used in optical laser experiments.¹⁸ For a Bragg spectrometer using a perfect crystal, it is difficult to measure such a broad energy range of x rays simultaneously due to reflections from multiple crystal planes and limited crystal size. The feasible operation is to ensure a sufficient spectral window around the central energy for each measurement. By shifting the central energy, the whole energy range can be covered by the spectrometer. The spectral window for each central energy is designed as ≥ 300 eV to allow for measurements of multiple emission lines and inelastic scattering. Moreover, the geometrical dimension of the spectrometer must be suitable for the interaction chamber IC1 of the HED instrument. The crystal has to keep a sufficient distance from the target to protect the crystal from debris from the target and avoid blocking other diagnostics. The chamber-limited source-to-detector distance also constrains the upper limit of source-to-crystal distance. Considering all factors, the source-to-crystal distance of the spectrometer is set as 150–450 mm. To summarize, the detailed requirements for the spectrometer design are as follows:

- Spatial resolution: 25 μm
- Spectral resolution: $\delta E < 5$ eV ($E/\delta E > 2000$)
- Covered energy range: 4–10 keV
- Spectral window: $\Delta E \geq 300$ eV
- Source-to-crystal distance: 150–450 mm

B. The crystal

To obtain high photon collection efficiency, based on the previous experience,^{12,13} a toroidally bent Ge crystal with a high integrated reflectivity is employed. The Ge 220 atomic plane with a lattice spacing $2d = 4.00$ Å is adopted to obtain the proper Bragg angles in the energy range of 4–10 keV. Considering the desired spectral range, space constraints, and manufacturing feasibility, the crystal size is chosen as $50 \times 25 \text{ mm}^2$ in the horizontal and vertical directions, respectively. The radii of curvature of the crystal are key parameters to determine the geometrical dimension, spatial resolution, and spectral window (or range) of the spectrometer. The radii of curvature are discussed and given in Sec. II C.

C. Geometrical analysis

To better understand and optimize the choice of the radii of curvature for the toroidal crystal spectrometer, the geometrical analysis of the system is implemented. The toroidal crystal actually acts as a Johann spectrometer¹⁹ along the horizontal (dispersive) plane while spatially focusing along the vertical (imaging) curvature. In general, the detector is located at the focus of the vertical curvature (i.e., sagittal focus) of the crystal for providing optimal spatial resolution.¹⁴ Furthermore, placing the detector tangentially on the Rowland Circle (RC) of the crystal improves the linearity of the dispersion and eliminates the source broadening.¹³ In an ideal case, we should ensure the sagittal focus is located on the RC

for optimal performance. A schematic of the focusing geometry of a toroidal crystal in the horizontal (meridional) plane is shown in Fig. 1.

For a crystal with a fixed curvature, placing the detector on the RC to measure lower energy x rays may cause too short source-to-crystal distance in a magnified geometry, which is necessary for the high spatial resolution. In addition, the spectral window on the detector may be too narrow due to the divergent reflected beam from the crystal. Consequently, for the design of this spectrometer, only the spatial focusing in the vertical plane is demanded, while the detector does not have to be on the RC as long as the spectrometer parameters meet the design requirements.

Vertical Curvature—For one-dimensional spatial focusing geometry, the vertical radius of curvature (R_v) of the crystal determines the dimension of the imaging spectrometer. The lensmaker's equation has to be satisfied for the vertical curvature,

$$\frac{1}{d_{sc}} + \frac{1}{d_{cd}} = \frac{1}{f_v}, \quad (1)$$

where d_{sc} is the source-to-crystal distance, d_{cd} is the crystal-to-detector distance, $f_v = R_v / (2 \sin \theta_B)$ is the vertical focal length, and θ_B is the Bragg angle. R_v can be derived from Eq. (1),

$$R_v = 2 \sin \theta_B d_{sc} \frac{M}{(M+1)}. \quad (2)$$

For a certain Bragg angle (θ_B) or x-ray energy (E), R_v is a function of the source-to-crystal distance (d_{sc}) and the spatial magnification ($M = d_{cd}/d_{sc}$). For a detector with the pixel size of d_{px} ,

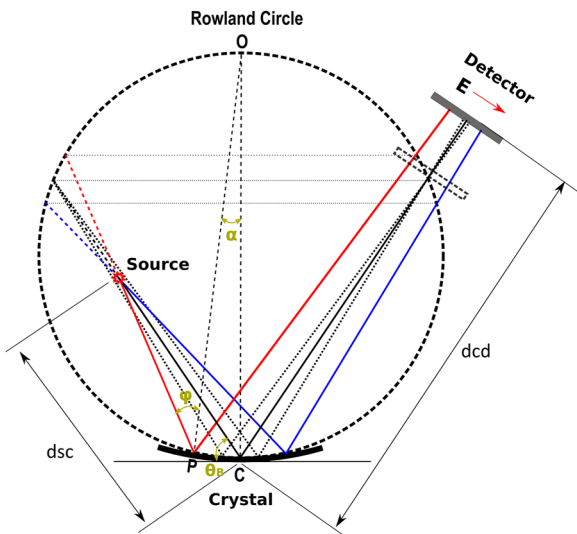


FIG. 1. Focusing property of a toroidal crystal in the horizontal plane with a chromatic, finite sized source located inside the Rowland circle. φ is the local incident angle relative to the local normal, θ_B is the Bragg angle on the crystal center, and α is the angle subtended by the crystal segment PC with respect to the point O .

each spatial resolution (δx) element is sampled over a number of pixels (N_s) on the detector,

$$N_s = \frac{M\delta x}{d_{px}}. \quad (3)$$

According to the Nyquist sampling theorem, the lower limit of the number of samples is $N_s > 2$. For a pixel size of $13.5 \mu\text{m}$ (e.g., Princeton Instruments PI-MTE camera) and a spatial resolution of $25 \mu\text{m}$, the magnification must meet $M > 1.08$. Here, a magnification of 1.5 is chosen to simplify the geometrical analysis.

Based on Eq. (2), with a change in the x-ray energy and d_{sc} value, the value of R_v varies as shown in Fig. 2. The R_v value in the range of 130–170 mm ensures that d_{sc} lies in the range of 150–450 mm for almost all x-ray energies in the 4–10 keV range when $M = 1.5$. To investigate the influence of magnification on the spectrometer dimension, d_{sc} values for different magnification and x-ray energies are also calculated, as illustrated in Fig. 3. For $R_v = 130 \text{ mm}$, d_{sc} is always in the range of 150–450 mm for x-ray energy of 5–10 keV. If selecting a smaller M value, e.g., 1.1–1.3, the d_{sc} value can also be in the range of 150–450 mm for lower x-ray energies (4–5 keV). Thus, $R_v = 130 \text{ mm}$ is chosen as the vertical radius of curvature of this spectrometer.

Horizontal Curvature—As the R_v value is fixed, distances of the source and detector relative to the crystal are given as well for a certain magnification. The choice of the horizontal curvature radius (R_h) determines the spectral range (window) and dispersion of the spectrometer. For a certain central energy (E) or Bragg angle (θ_B), the spectral range ΔE is estimated by the following equation.¹⁴

$$\Delta E = \frac{hc}{2d} \left[\frac{1}{\cos \varphi_{\max}} - \frac{1}{\cos \varphi_{\min}} \right], \quad (4)$$

where h is the Planck constant, c is the speed of light, d is the lattice spacing, and φ is the local incident angle of x rays relative to the local normal on the crystal surface. φ can be given by $\varphi = \pi/2 - \theta_B - \left(\frac{d_{sc} - R_h \sin \theta_B}{d_{sc}} \right) \cdot \alpha$, and α is the angle subtended by a segment of crystal with respect to the center of the horizontal curvature. Both φ and α are illustrated in Fig. 1. Thus, φ_{\max} and

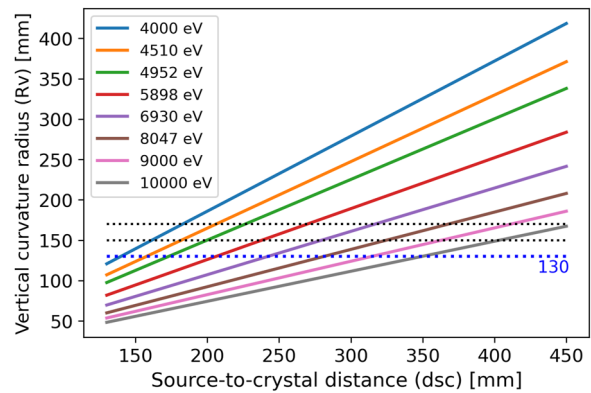


FIG. 2. Vertical radius of curvature (R_v) changes with source-to-crystal distance (d_{sc}) at $M = 1.5$ for different photon energies. The dotted lines denote $R_v = 130$, 150, and 170 mm respectively.

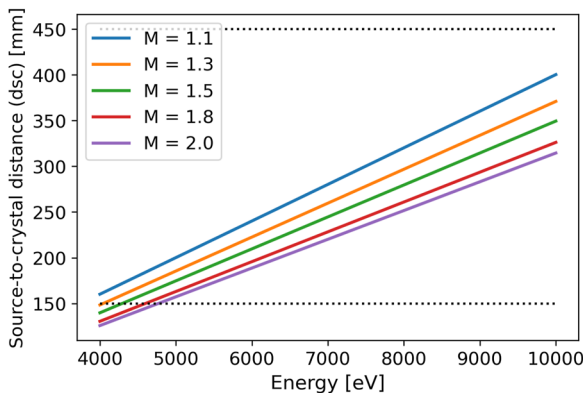


FIG. 3. Source-to-crystal distances at different magnifications (M) and photon energies (E) for $R_v = 130$ mm. The dotted lines denote $d_{sc} = 150$ and 450 mm.

φ_{\min} are the local incident angles at the edges of the crystal in the horizontal plane, corresponding to the maximum and minimum of the angle α . Assuming the crystal dimension is much smaller than the horizontal radius of curvature, $\alpha \sim \sin \alpha \sim L/R_h$ is obtained, so the maximum and minimum of the angle α are $\pm(L_c/2)/R_h$, respectively. L_c is the crystal dimension along the horizontal direction, i.e., $L_c = 50$ mm. Consequently, the spectral range ΔE is a function of the central energy E , source-to-crystal distance d_{sc} , horizontal curvature radius R_h , and crystal length L_c .

To optimize the value of R_h , spectral ranges for d_{sc} in the 150–450 mm range and central energy in the 4–10 keV range are calculated. As an example, Fig. 4 shows the calculation results for $R_h = 1200$ mm and $R_h = 1800$ mm. In Fig. 4(a), the dropping peak represents that the source is exactly on the RC, and the left side of the peak means the source is inside the RC, whereas the right side means the source is outside the RC. For a Johann spectrometer, if the source is located farther away from the RC, the spectral range will be broader, and if the source is located on the RC, the instrument will serve as a monochromator.

If the source lies outside the RC, the detector will be outside and farther from the RC due to the resolution constraint $M > 1$. In this case, even though the spectral range meets the requirement, the effect of source broadening will be stronger, usually resulting in lower spectral resolution and signal-to-noise ratio. Moreover, if the source lies inside the RC, the source broadening will be reduced to some extent in the magnified geometry. Experiments have shown that low-density plasma may blow around the shielding, leading to source broadening that distorts the scattered spectrum.¹³ Consequently, the source should always be put inside the RC for all x-ray energies and kept at a sufficient distance from the RC.

The crystal with a larger R_h has a bigger RC, and thus, the source is more likely located inside the RC and the distance from the source to the RC is longer when the d_{sc} is limited ($d_{sc} \leq 450$ mm). Figure 4(b) shows that, selecting $R_h = 1800$ mm, the source lies inside the RC for all x-ray energies in the 4–10 keV range, and the spectral range also meets the design requirement. Thus, $R_h = 1800$ mm is selected as the horizontal radius of curvature. To further investigate this option, ray-tracing simulations are necessary to precisely evaluate the parameters of the spectrometer.

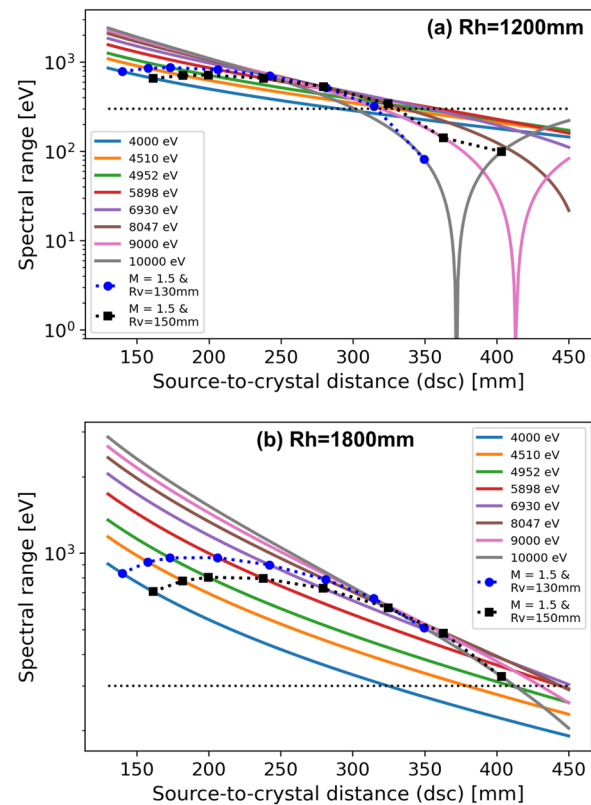


FIG. 4. Spectral range changes with source-to-crystal distance for different central photon energies when (a) $R_h = 1200$ mm and (b) $R_h = 1800$ mm. Each color solid line, corresponding to a central energy, shows the variation of spectral range along d_{sc} . The blue circle and black square on the curve, respectively, denote d_{sc} and the spectral range for $R_v = 130$ mm and $R_v = 150$ mm when $M = 1.5$, so the circle/square dotted lines show the variations of the spectral range along the central energy in two cases. The horizontal dotted line denotes the spectral range of 300 eV.

D. Ray-tracing simulations

To evaluate and optimize the performance of the spectrometer, ray-tracing simulations for various configurations are implemented with the code *mmpxrt*.²⁰ As shown in Fig. 5, the theoretical performance of spectrometers with different radii of curvature are compared. These simulations are set for the detector with a pixel size of $13.5 \mu\text{m}$ and a chip size of $27 \times 27 \text{ mm}^2$. To simplify the analysis, the detector is set by default to be perpendicular to the reflected beam from the crystal.

In Fig. 5, the spectral resolution (δE) is defined as the full-width-at-half-maximum (FWHM) of the point spread function (PSF) profile, the spectral range refers to the energy range of photons collected by the detector, and the efficiency is calculated as the ratio of the number of detected photons to the total of emitted photons from an isotropic point source. Both spectral resolution and efficiency are evaluated for each central energy by the simulation with a monochromatic source. The spectral range is evaluated from the simulation with a broadband source centered at a certain energy.

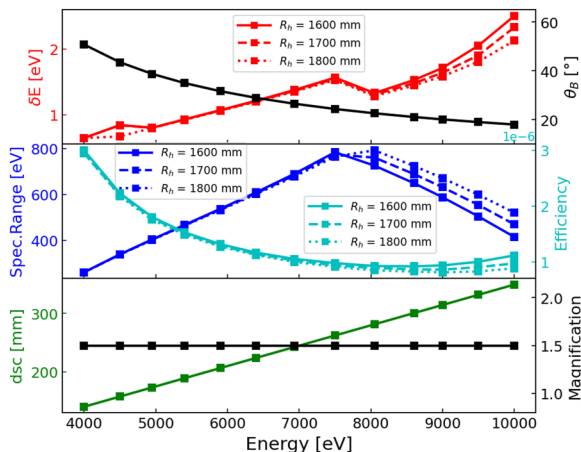


FIG. 5. Theoretical performance of Ge (220) spectrometers with a fixed $R_v = 130$ mm and different $R_h = 1600, 1700$, and 1800 mm for the energy in the 4–10 keV range. The spectral range probably will be reduced if the detector is set with various angles relative to the reflected beam.

When R_v is fixed, for larger R_h , both spectral resolution (δE) and spectral range are improved while the efficiency gets slightly lower. This trend is only obvious for higher energies.

The measured spectral range is also affected by the detector size. For lower x-ray energies (4–8 keV), the reflected beam from the crystal is divergent, and only a part of reflected photons can hit the detector, as shown in Fig. 6. In this case, the spectral range is mainly limited by the detector size, not R_h ; thus, the spectral ranges for three R_h values are almost identical. As the central energy increases from 4 keV, the reflected beam gets less and less divergent until convergent, which increases the spectral range with the energy in the range of 4–8 keV. When all reflected photons can hit the detector (8–10 keV), the spectral range is dominated by the distance from the source to the RC, and the source gets closer to the RC with the central energy increasing. A larger R_h makes the source

farther away from the RC and, thus, presents a broader spectral range.

The change in the spectral resolution (δE) with the central photon energy is due to the worsening of focusing and increasing spectral dispersion (dE/dx). In the energy range of 4–8 keV, the divergent reflected beam guarantees a sufficiently small dispersion on the detector. In this case, the limited increase in R_h has little influence on the dispersion, and thus, the spectral resolutions are almost the same for three R_h values. As the energy increases to 8–10 keV, the convergent reflected beam results in an even larger dispersion, which makes the spectral resolution sensitive to the variation of R_h . Thus, increasing R_h can alleviate the increase in the dispersion to improve the spectral resolution. The spectral resolution of ≤ 2.5 eV is always obtained at 4–10 keV for $R_h = 1800$ mm, i.e., $E/\delta E \geq 4000$. The dependence of efficiency on central energy is mainly due to two factors. First, d_{sc} increases with the energy, resulting in a smaller solid angle subtended by the crystal with respect to the source. Second, with the incident photon energy varying from 4 to 10 keV, the integrated reflectivity of Ge (220) crystal decreases from ~ 186 to $\sim 58 \mu\text{rad}$, as calculated by the X-ray OPTics utilities (XOP).²¹ The change in R_h has little influence on efficiency. The calculated efficiency of this spectrometer is approximately one order of magnitude lower than that of the HAPG spectrometers.¹⁷

Based on ray-tracing simulations,²⁰ Ge (220) crystal with radii of curvature of $R_v = 130$ mm and $R_h = 1800$ mm meets all the design requirements, especially guaranteeing a sufficiently high spectral resolution at 9–10 keV. To achieve the best spatial resolution, the spectrometer must be aligned accurately, ensuring that the spectrum is focused over the whole detected energy region. In most cases, the spectrum is only focused on a small region and spreads out at the ends. Consequently, the detector has to be aligned to a certain angle with respect to the reflected beam. Ray-tracing simulations can also be used for assessing the orientation of a detector to achieve the best focusing. Figure 7 shows the simulated images on the detector for different rotations, where 0° corresponds to the detector perpendicular to the reflected beam and positive angles indicate the rotation direction making higher energy x rays have a long distance from the crystal to the detector than lower energy x rays. The optimal angle of 60° is obtained for the setup of central energy 9 keV and magnification 1.5. The FWHM of the best focused spatial profile is $18 \mu\text{m}$, implying a spatial resolution of $\sim 12 \mu\text{m}$ on the target coordinates. The simulations also provide an estimation of the needed alignment precision, i.e., $\pm 2^\circ$, for the detector rotation. This work has to be performed for each specific experiment because the optimal rotation angle varies with the geometrical configuration and central photon energy, and no analytical formula exists for it.

E. Technical design

1. “Curved-rail” version

There are two technical designs for various applications of the spectrometer in different scenarios. The spectrometer is first designed to be mounted on the curved-rail system in the interaction chamber IC1 of the HED instrument, as shown in Fig. 8. Both crystal and detector are mounted on motorized stages moving along the curved rails centered on the target chamber center (TCC), allowing the entire spectrometer to be placed at varied angles with respect to the TCC. In addition, both the crystal and detector are

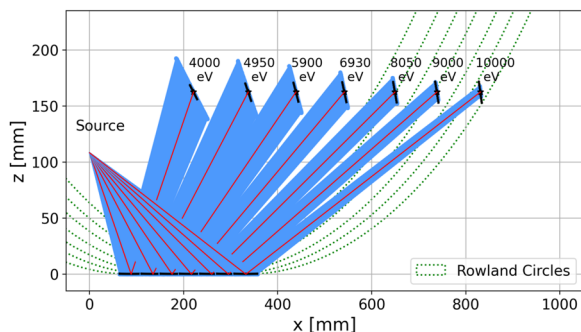


FIG. 6. Side views of the Ge (220) spectrometer with the radii of curvature of $R_v = 130$ mm and $R_h = 1800$ mm. The red lines denote x rays with the central energies, the blue lines are the corresponding continuous spectra, and the green curves represent the Rowland circles for the crystal located at different positions on the x axis. The detectors (black lines) are perpendicular to reflected central energy x rays (red lines), despite the angles distorted by the image scale.

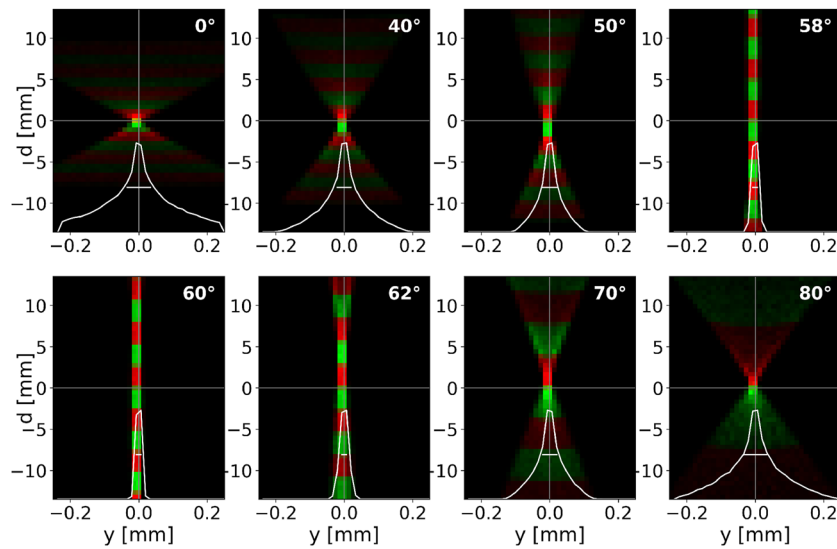


FIG. 7. Simulated images of Ge (220) spectrometer for 9 keV central energy and various rotations of the detector, showing that the detector rotation between 58° and 62° provides the best focusing. The red and green strips are changing each 50 eV to show the spectral range on the detector. The white curves show the spatial (horizontal) profiles of all detected photons, and the white straight lines denote the FWHMs of spatial profiles.

equipped with motorized linear and rotation stages. Two linear stages are always positioned along the radial direction of the curved rails so that the source-to-crystal and source-to-detector distances are both adjustable. Two rotation stages are used for adjusting the angles of the crystal and detector in the dispersive plane with respect to the incoming beams. A goniometer is also used in the crystal positioning system for adjusting the crystal angle in the imaging direction. In this way, the spectrometer can be aligned in vacuum by using x rays, and the spectrometer configuration can also be changed to observe x rays of different energies without breaking the vacuum.

The design details of the crystal and detector positioning systems are shown in Fig. 9. A pokalon foil is put in front of the crystal as the debris shield. The camera head is usually covered by a pokalon foil as the light-tight filter or other attenuating foils

(e.g., aluminum) as the x-ray filter. In the XFEL-only experiments, this shielding measure is sufficient to block the background light. However, in the optical laser-solid interaction experiments, much stronger, more complicated background radiation arises due to the hot electron production. Therefore, a specific shielding design is needed for the spectrometer. As shown in Figs. 9(a) and 9(b), a specific camera bracket combined with a collimating tunnel (or collimator) is designed to significantly improve the shielding of the background radiation. The collimator is aimed at limiting the field of view of the camera and is always aligned along the incoming beam. The camera can be adjusted to a certain angle with respect to the collimator by the rotation stage and a special link structure. Modular tungsten plates with a thickness of 2 mm are manufactured to be mounted on the surface of the camera bracket and the internal surface of the collimator, which protects the sensor from irradiation by secondary radiation. Four small tungsten plates are used to adjust the slit aperture of the collimator. In addition, two 25 mm thick lead blocks enveloped by aluminum plates, denoted as the direct beam block and view block, respectively (as seen in Fig. 8), are prepared to improve the shielding further. The direct beam block is placed between the TCC and the detector to block the direct field of view of the TCC toward the detector, preventing the laser-induced electrons and photons from hitting the camera and producing secondary radiation in it. The view block is put behind the crystal, preventing the secondary radiation coming from the back of the crystal from penetrating the collimator.

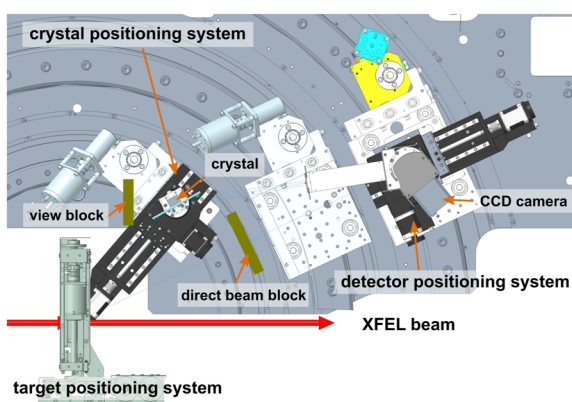


FIG. 8. A schematic of the Ge spectrometer in the IC1 of the HED instrument, European XFEL. The crystal and detector positioning systems are mounted on different curved rails of IC1, which allows changing the geometrical configuration by using motors. The detector is rotated to an angle clockwise.

2. “Self-standing” version

To improve the flexibility of the spectrometer, a “self-standing” version of this spectrometer is designed, as shown in Fig. 10. The crystal and camera positioning systems are mounted onto two independent posts, which are movable according to the spectrometer geometry. The linear translation stage for the crystal is removed to simplify the structure around the interaction point. The position and orientation of the crystal relative to the source can be adjusted

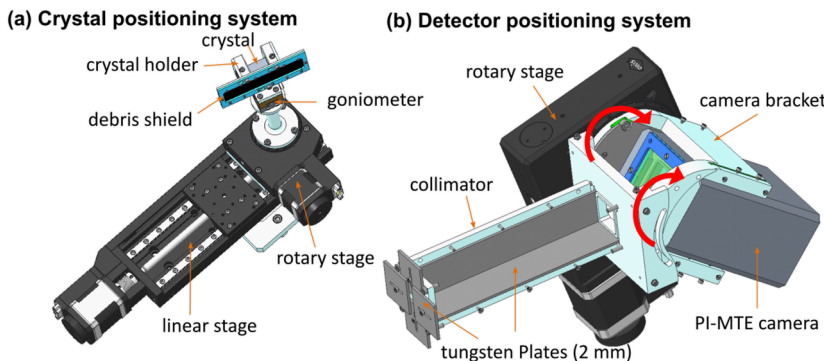


FIG. 9. Design of (a) crystal positioning system and (b) detector positioning system for the Ge spectrometer.

roughly by moving the post and adjusting the crystal height. The axis of the linear stage of the detector can be defined by a rotary disk (blue in Fig. 10), instead of the curved rail in the first version of the spectrometer. The high flexibility allows its use with other diagnostics in various experimental scenarios.

3. Detectors

Different x-ray detectors can be used in the design of the spectrometer. The first is the high-sensitivity PI-MTE camera from Teledyne Princeton Instruments.²² The PI-MTE camera incorporates a back-illuminated, deep-depletion CCD [without anti-reflective (AR) coating], which contains a 2048×2048 imaging array of $13.5 \times 13.5 \mu\text{m}^2$ pixels. With the 100% fill factor, the camera offers a large imaging area ($27.6 \times 27.6 \text{ mm}^2$). This camera allows for high spatial resolution due to the small pixel size. Combined with a liquid-assisted thermo-electric cooling system, the PI-MTE camera can work in a high-vacuum environment over a long operation time. The lowest cooling temperature of -50°C ensures a significant reduction of the dark current or noise. Another highlight of this camera is its good electromagnetic pulse (EMP) resilience, which enables it to be used during high-power optical laser-matter interaction experiments. The second one is the ePix100 detector. Currently, two vacuum-compatible ePix100 modules¹⁷ are available to users in the HED instrument of

European XFEL, which have a pixel size of $50 \mu\text{m}$, a detection area of $35 \times 38 \text{ mm}^2$, a dynamic range of 10^3 photons per pixel at 8 keV, and a repetition of 120 Hz. The ePix100 detector limits the spatial resolution by the larger pixel size but allows for high repetition operation.

III. EXPERIMENTAL RESULTS

A. Calibration experiments at the microfocus x-ray source

To verify the spectrometer performance with respect to its spectral and spatial resolution, calibration experiments were carried out with the microfocus x-ray source (XS225D) at the ELBE, Center of Helmholtz-Zentrum, Dresden-Rossendorf (HZDR). The tungsten x-ray tube provided an x-ray source with a minimum spot size of $\sim 5 \mu\text{m}$ and a beam divergence of 25° . The spectrometer was first set to observe the L-shell characteristic x rays of tungsten. The central energy was selected as 9672 eV (Bragg angle $\theta_B = 18.69^\circ$) to cover the most pronounced W L β lines. The crystal was placed on the beam axis of the radiation cone of the x-ray tube. The source-to-crystal distance was 338 mm, and the crystal-to-detector distance was 507 mm, as required by the focusing geometry for the magnification of 1.5. The detector used was the PI-MTE CCD camera, covered by a pokalon foil as the light-tight filter. Based on ray-tracing simulations, the detector was rotated by 50° with respect to the reflected beam for the best focusing.

The measured tungsten spectrum is shown in Fig. 11. The L β 1, L β 2, L β 3, and L β 4 lines were observed and identified. These transition lines were used to fit the energy dispersion of the spectrometer in this configuration, as shown in Fig. 12. The fitted dispersion was in perfect agreement with the result from the ray-tracing simulation, demonstrating an approximate linear dispersion. To evaluate the spectral resolution, the linewidths of the measured L-shell transitions were estimated. For a cold x-ray source, the lines were broadened by several effects, including natural linewidth, source broadening, and instrumental broadening. Due to the fact that the strongest L β 1 and L β 2 lines were saturated or overlapped with other lines, the best focused L β 4 line was chosen for evaluating the spectral resolution, as shown in Fig. 13. The measured L β 4 linewidth (FWHM) was estimated as $\sim 16.5 \text{ eV}$. A source broadening of $\sim 0.14 \text{ eV}$ was approximately determined by the ray-tracing simulated source-size dispersion of 14 eV/mm and the assumption of $10 \mu\text{m}$

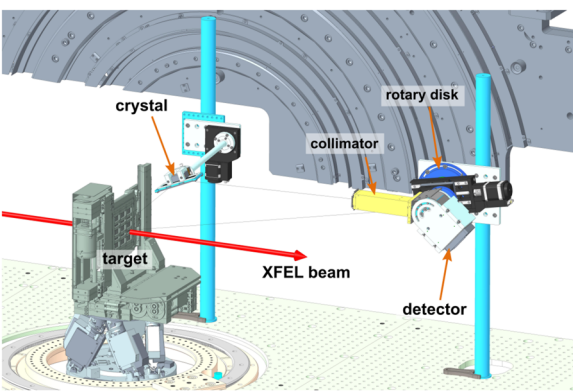


FIG. 10. A schematic of the self-standing version of the Ge spectrometer in the IC1 of the HED instrument, European XFEL. The detector is rotated to an angle clockwise.

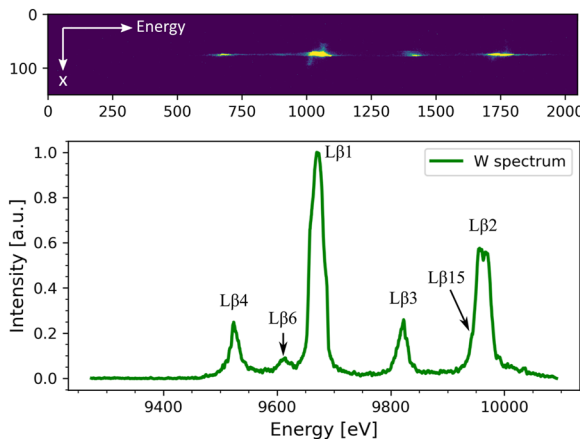


FIG. 11. L-shell characteristic x-ray spectrum from the tungsten x-ray tube measured by the Ge spectrometer.

source size (justified below), indicating that the source broadening was negligible. The natural linewidth referred to the precision measured value (13.2 eV) of the W $L\beta 4$ linewidth in the Advanced X-ray Astrophysics Facility (AXAF) Project Science.²³ An asymmetrical PSF profile from ray-tracing simulations was used in the evaluation of the spectral resolution, labeled as the simulated PSF in Fig. 13. By scaling the width of the PSF, the convolution of the natural spectrum and simulated PSF was fitted to the measured spectrum. An FWHM of the PSF of ~ 3.8 eV, i.e., instrumental broadening, was obtained from the best fit, implying a spectral resolving power of ~ 2500 .

To evaluate the spatial resolution, the spectrally integrated, spatial profile of the unsaturated region of the measured spectrum was plotted. This profile had an FWHM of $\sim 36 \mu\text{m}$, corresponding to a spatial size of $24 \mu\text{m}$ in the source plane. The precise x-ray source size was uncertain, but its range was estimated as $5\text{--}17 \mu\text{m}$ by the calibration. Thus, the x-ray source size was reasonably assumed to

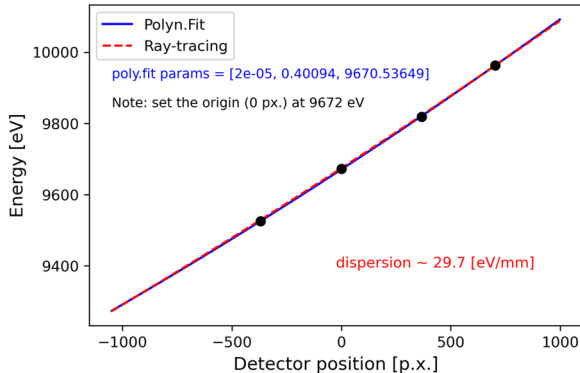


FIG. 12. Dispersion of the spectrometer. Black dots are experimental data, i.e., positions of the identified lines, the blue curve is the polynomial fit to the experimental data, and the red dash curve is the dispersion from the ray-tracing simulation. An approximate linear dispersion of ~ 29.7 eV/mm is obtained at the origin.

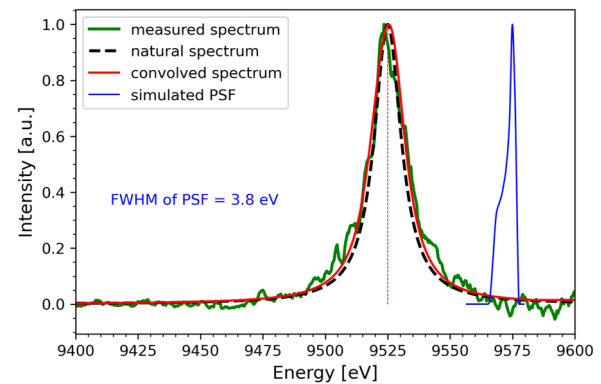


FIG. 13. The spectral resolution evaluation using the measured W $L\beta 4$ line (green). The natural spectrum (black) is a Lorentzian profile with an FWHM of 13.2 eV. The convolved spectrum (red) is the best fit to the measured spectrum, i.e., the convolution of the natural spectrum and a simulated PSF (blue) with an FWHM of 3.8 eV.

be $10 \mu\text{m}$. The spatial resolution was estimated by fitting a simulated profile to the spatial profile of the measured W lines. The simulated profile was the convolution of a one-dimensional source profile and a Gaussian PSF. The source profile was assumed to be a rectangle profile with a width of $10 \mu\text{m}$. The best fit indicated that the FWHM of the spatial PSF was $\sim 24 \mu\text{m}$ for the unsaturated lines. If considering only the best-focused region (single line) of the measured spectra, a better spatial resolution of $\sim 19 \mu\text{m}$ was achieved, as shown in Fig. 14. From the Nyquist theorem, the lower limit on the spatial resolution is expected to be $18 \mu\text{m}$ for this setup. This result indicates that the spectrometer is focused perfectly in a small region but not in the whole spectral region. In this case, the spatial resolution is mainly limited by the detector pixel size, spatial magnification, and focusing error.

In addition, the spectrometer was also set to measure the copper (Cu) $K\alpha$ spectrum by backlighting a Cu grid with the W x-ray tube. The experimental setup is illustrated in Fig. 15. The Cu grid was

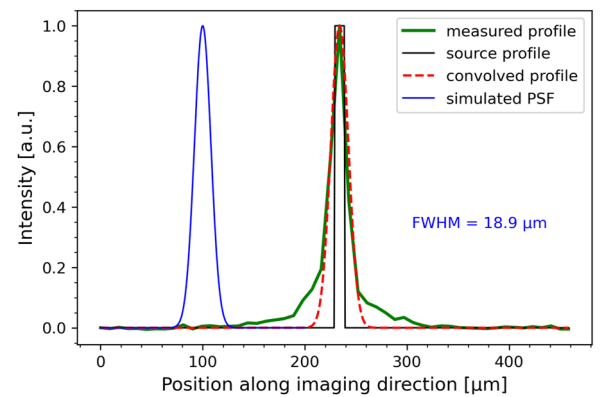


FIG. 14. The spatial profile of the best-focused region of the measured spectrum (green) and the deduction of the spatial resolution. The convolved profile (red) is the best-fitted profile, which is the convolution of the source profile (black) and a Gaussian PSF (blue) whose FWHM is $18.9 \mu\text{m}$. The spatial profile has been switched into the source coordinates.

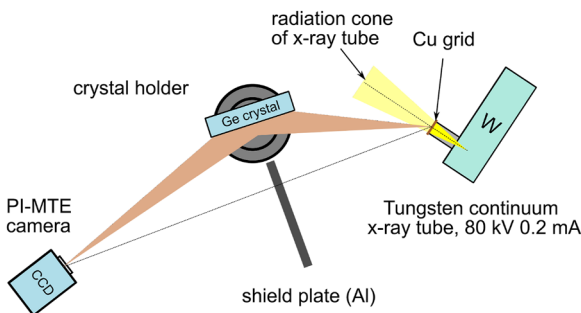


FIG. 15. Schematic setup for the illumination of the Ge crystal by a Cu fluorescence target.

attached to the aperture surface of the x-ray tube, and the x-ray fluorescence of Cu was excited by the W continuum x-rays, with a source size as same as the aperture. The crystal was put out of the radiation cone of the x-ray tube to prevent intense W x-rays from covering the Cu $\text{K}\alpha$ signal. The Cu fluorescence was assumed to be illuminating the crystal isotropically. To obtain sufficient $\text{K}\alpha$ photons, the exposure time was set to 10 min. The spectrometer was centered at 8047 eV ($\theta_B = 22.65^\circ$), with a source-to-crystal distance of 281 mm and the crystal-to-detector distance of 422 mm, keeping the magnification at 1.5. Due to the small spectral window, the spatial focusing of Cu $\text{K}\alpha$ was achievable when the detector was put perpendicular to the reflected beam. A 2 mm thick aluminum plate was placed between the source and detector to shield the direct radiation from the Cu target.

The Cu grid used in the experiments had parallel bars with 28 μm bar width and 63 μm center-to-center spacing, as shown in Fig. 16(a). The spectrometer was focused on the grid, and the non-dispersive plane was perpendicular to these parallel bars so that the “modulated” Cu $\text{K}\alpha$ emission was imaged by the crystal onto the detector. The one-dimensional spatially resolved $\text{K}\alpha$ spectrum from the Cu grid is shown in Fig. 16(b). Both $\text{K}\alpha 1$ and $\text{K}\alpha 2$ were seen, but they were partially overlapped because of the source broadening. Stripes representing x rays from the Cu bars were visible in the image, as well as the rim of the grid. The spatial extension of the $\text{K}\alpha$ image was about 3.7 mm, corresponding to a field of view of at least

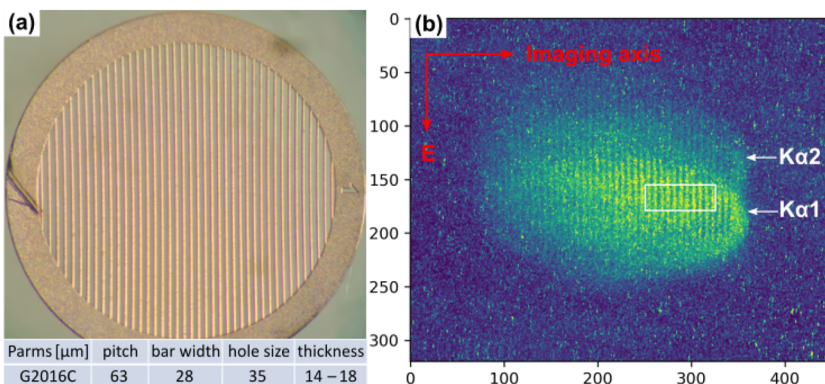


FIG. 16. (a) The Cu grid used in the experiments and (b) the Cu $\text{K}\alpha$ image measured by the spectrometer. In (a), the target parameters are given, and the parallel bars are aligned perpendicular to the imaging axis during the experiments. For (b), the imaging axis is along the horizontal direction and the dispersive axis is along the vertical one. The white box shows the selected region for the spatial resolution evaluation.

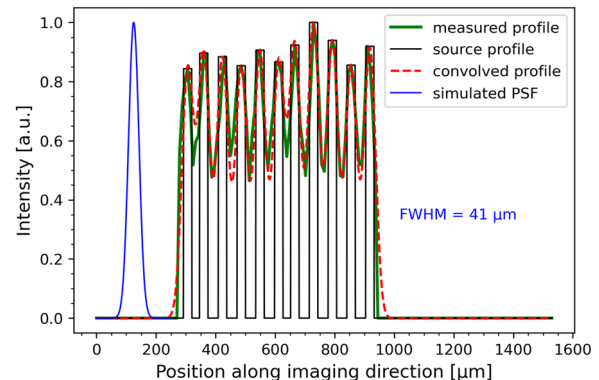


FIG. 17. The spatial profile of the selected Cu $\text{K}\alpha$ image (green) and the deduction of the spatial resolution. The convolved profile (red) is the best-fitted profile, which is the convolution of the source profile (black) and a Gaussian PSF (blue) whose FWHM = 41 μm . The spatial profile has been switched into the target coordinates.

2.47 mm on the target, as well as in good agreement with the aperture size of x ray tube of 2.5 mm. Due to the inhomogeneity of the $\text{K}\alpha$ emission of Cu bars, the spacing of the strips tended to be blurred in the edge region. Therefore, only the prominent stripe region was selected for the spatial resolution evaluation.

The spatial profile of the selected Cu $\text{K}\alpha$ image is shown in Fig. 17. To infer the spatial resolution, a one-dimensional source profile representing the x-ray emission from the grid was first constructed approximately, as shown by the black curve in Fig. 17. It consisted of a series of rectangle profiles that have the same amplitudes as the corresponding peaks and the same width as the Cu bar size. The source profile was convolved with a Gaussian PSF, then fitted to the measured spatial profile. The best fit gave an FWHM of the PSF of 41 μm . This spatial resolution is worse than that of the previous evaluation. Except for the alignment error, the big difference may be the consequence of two effects. The first effect comes from the deviation between the artificial and real source profiles. The inhomogeneous emission of Cu bars has been observed in Fig. 16, so the real source profile should not be rectangles with sharp edges but with smooth edges. However, the real source profile is unknown. When the source profile was set with smooth edges, a better spatial resolution (e.g., 36 μm) could be evaluated by using the same

method. The second effect comes from the broadening of the source perpendicular to the source-to-crystal vector and imaging axis. The image becomes defocused as the spatial resolution elements move off the imaging axis.¹² The source size in the dispersive direction was estimated as ~ 1.9 mm, and the spatial resolution could be degraded significantly by the effect of source broadening. Thus, the actual spatial resolution of the spectrometer is found to be better than $41\ \mu\text{m}$ in this configuration.

B. Measurements of Cu K β spectra at the HED instrument of European XFEL

The first application of the Ge spectrometer at the HED instrument of European XFEL was to measure the K β emission from the Cu target heated by the XFEL beam, investigating the atomic processes during isochoric heating of mid-Z elements in conjunction with other diagnostics. The spectrometer was centered at 9050 eV ($\theta_B = 22.03^\circ$), set with a source-to-crystal distance of 320 mm and a crystal-to-detector distance of 466 mm, having a spatial magnification of 1.46. The ePix100 detector was used in the experiment for the high repetition operation. To spatially focus the whole recorded spectra, the detector was rotated by 48° with respect to the reflected beam, as shown in Fig. 18. Due to the relatively clean background radiation in the presence of only XFEL, the detector was only shielded by the pokalon foil used as the light-tight filter. The dispersive plane of the spectrometer was set off the axis of the XFEL beam to avoid interfering with other diagnostics.

The XFEL beam was operated at 10 Hz repetition and focused to a spot of $\sim 5\ \mu\text{m}$ diameter on the target. The running time was set to 200 s, generating 2000 shots in the run. All the spectra presented here were averaged over all shots in each run. Cu K β spectra with numerous satellites were measured by the spectrometer during the experiment, as shown in Fig. 19. The elastic scattering of the XFEL was measured as well, which could be used as the additional energy calibration. For evaluating the spectral resolution in this configuration, the XFEL beam with only $\sim 20\ \mu\text{J}$ pulse energy was selected, providing an intensity in the order of $10^{15}\ \text{W/cm}^2$ on the target. The

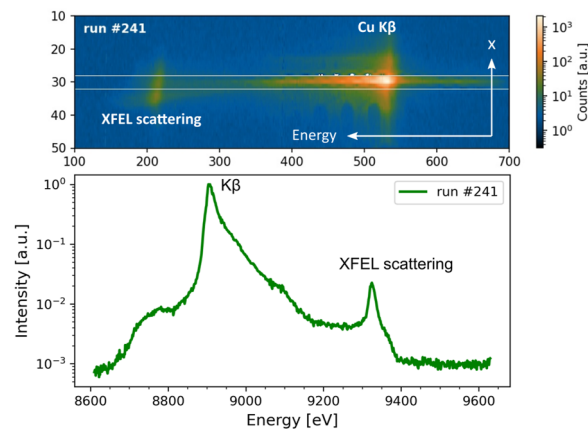


FIG. 19. A typical heated spectrum measured by the spectrometer. A $3\ \mu\text{m}$ thick Cu foil was heated by the XFEL beam sufficiently to produce K β satellites. The elastic scattering of XFEL photons was also measured.

Cu sample was only heated to an electron temperature of ~ 1 eV, as simulated by the SCFLY code.²⁴ Thus, the effect of Doppler broadening on the linewidth was negligible. The spectral lineout of the cold Cu K β is shown in Fig. 20, presenting an FWHM of ~ 9 eV. By comparing with the reference value (5.92 eV)²⁵ of the natural linewidth of Cu K β , an instrumental broadening of ~ 6.5 eV was estimated by the same method. This spectral resolution ($E/\delta E \approx 1400$) is lower than the previously inferred value (2500), mainly arising from the bigger pixel size of the ePix100 detector. This spectral resolution is also lower than the prediction from the ray-tracing simulation, i.e., 3.4 eV. Several factors may affect the measured spectral resolution. The first is potential deficiencies in the alignment, i.e., alignment error. It is more difficult to precisely focus the spectrum for the detector with a larger pixel size because the pixel size determines the minimal spatial width of the observed spectrum.

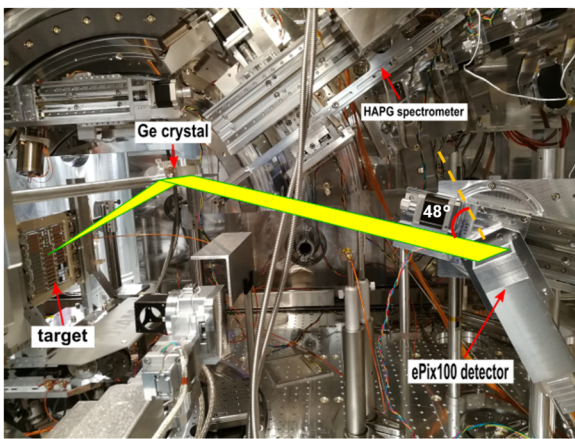


FIG. 18. The setup of the "self-standing" Ge spectrometer mounted in the IC1 chamber at the HED instrument of the European XFEL. The detector is rotated clockwise.

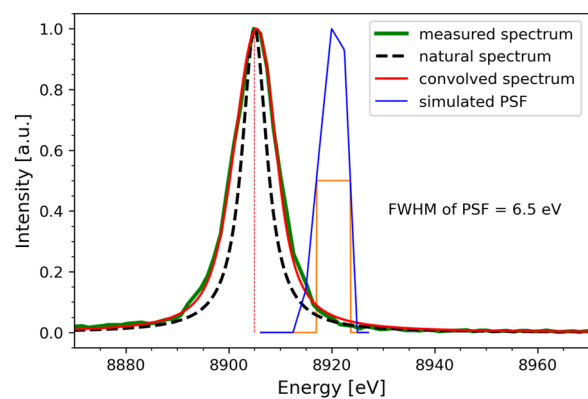


FIG. 20. The spectral lineout of the cold Cu K β from the target illuminated by the XFEL beam with $\sim 20\ \mu\text{J}$ pulse energy (green). The natural spectrum (black) is a Lorentzian profile with an FWHM of 5.92 eV. The convolved spectrum (red) is the best fit to the measured spectrum (green), i.e., the convolution of the natural spectrum and a simulated PSF with an FWHM of 6.5 eV.

In addition, the imperfections of the crystal will also affect the spectral resolution by introducing more aberrations for the focusing of x rays. Due to time and technical constraints, the dependence of spectral resolution on the detector tilt angle was not measured.

IV. CONCLUSION

The imaging x-ray spectrometer with a toroidally curved Ge crystal is developed for the HED instrument of the European XFEL. The spectrometer provides high-resolution, space-resolved spectral measurements for x rays in the energy range of 4–10 keV. Combining the high integrated reflectivity of Ge crystals, this imaging spectrometer is a powerful tool to diagnose spatially inhomogeneous plasmas with large, one-dimensional gradients in temperature, density, and ionization state.

A spectral resolution of ~ 3.8 eV at 9525 eV (i.e., $E/\delta E \approx 2500$) and a spatial resolution of $\sim 19\ \mu\text{m}$ are demonstrated experimentally when the spectrometer coupled with the PI-MTE camera was set to the magnification of 1.5. Other parameters, e.g., a field of view of 2.5 mm and a spectral window of ~ 560 eV, are also demonstrated, which meet the design requirements. For the spectrometer coupled with the ePix100 detector, a spectral resolution of ~ 6.5 eV at 8905 eV, i.e., $E/\delta E \approx 1400$, is demonstrated for the magnification of 1.5. Taking the experimental errors into account, these measured values are in good agreement with the prediction of ray-tracing simulations. According to the experimental results and analysis, several factors affect the spectral and spatial resolution, including the accuracy of the alignment, the pixel size of detectors, the spatial magnification, and the intrinsic properties and imperfections of the crystal. Precise alignment improves both spectral and spatial resolution by minimizing the aberration of x rays. To achieve a higher spatial resolution, a larger magnification and a smaller detector pixel are suggested. However, too large magnification may cause strong astigmatism in the imaging. Limiting the width of the crystal in the imaging direction can also enhance the spectral and spatial resolution due to the reduced spherical aberration but at the expense of detection efficiency or signal intensity.

The spectrometer has been tested in the high energy region (9–10 keV), demonstrating excellent performance. According to the tendency of the performance predicted by the ray-tracing simulations, higher spectral resolution is expected in the low energy region (4–9 keV). In addition, lower x-ray energies usually result in less focusing error due to the decreased distances and aberrations, so higher spatial resolution is also expected at lower energies. In summary, this spectrometer promises excellent spectral and spatial resolution in a wide energy range. It can be applied in various experimental scenarios, such as XRTS measurements for dense plasmas, x-ray emission, and absorption spectroscopy.

ACKNOWLEDGMENTS

We acknowledge European XFEL in Schenefeld, Germany, for the provision of x-ray free-electron laser beamtime at the HED instrument and would like to thank the staff for their assistance. We would also like to thank Natalia Shevchenko at the HZDR for providing the microfocus x-ray source. This work was funded by Helmholtz Association under Grant No. VH-NG-1338.

AUTHOR DECLARATIONS

Conflict of Interest

The authors have no conflicts to disclose.

Author Contributions

X. Pan: Conceptualization (equal); Data curation (lead); Formal analysis (lead); Investigation (lead); Methodology (lead); Project administration (equal); Software (lead); Validation (lead); Visualization (lead); Writing – original draft (lead); Writing – review & editing (lead). **M. Šmid:** Conceptualization (equal); Data curation (equal); Formal analysis (equal); Investigation (equal); Methodology (equal); Project administration (equal); Writing – review & editing (equal). **R. Štefaníková:** Data curation (supporting); Investigation (supporting). **F. Donat:** Visualization (lead). **C. Baehitz:** Data curation (supporting). **T. Burian:** Data curation (equal). **V. Cerantola:** Data curation (equal). **L. Gaus:** Data curation (equal). **O. S. Humphries:** Data curation (supporting); Writing – review & editing (supporting). **V. Hajkova:** Data curation (supporting). **L. Juha:** Data curation (supporting). **M. Krupka:** Data curation (supporting). **M. Kozlová:** Data curation (supporting). **Z. Konopkova:** Data curation (supporting). **T. R. Preston:** Data curation (supporting). **L. Wollenweber:** Data curation (supporting). **U. Zastrau:** Data curation (supporting); Writing – review & editing (supporting). **K. Falk:** Conceptualization (equal); Data curation (equal); Formal analysis (equal); Funding acquisition (lead); Investigation (equal); Methodology (equal); Project administration (equal); Supervision (lead); Visualization (equal); Writing – review & editing (equal).

DATA AVAILABILITY

The data that support the findings of this study are available from the corresponding author upon reasonable request.

REFERENCES

- ¹S. H. Glenzer, G. Gregori, R. W. Lee, F. J. Rogers, S. W. Pollaine, and O. L. Landen, *Phys. Rev. Lett.* **90**, 175002 (2003).
- ²S. H. Glenzer, G. Gregori, F. J. Rogers, D. H. Froula, S. W. Pollaine, R. S. Wallace, and O. L. Landen, *Phys. Plasmas* **10**, 2433 (2003).
- ³S. H. Glenzer, O. L. Landen, P. Neumayer, R. W. Lee, K. Widmann, S. W. Pollaine, R. J. Wallace, G. Gregori, A. Höll, T. Bornath, R. Thiele, V. Schwarz, W.-D. Kraeft, and R. Redmer, *Phys. Rev. Lett.* **98**, 065002 (2007).
- ⁴L. B. Fletcher, U. Zastrau, E. Galtier, E. J. Gamboa, S. Goede, W. Schumaker, A. Ravasio, M. Gauthier, M. J. MacDonald, Z. Chen, E. Granados, H. J. Lee, A. Fry, J. B. Kim, C. Roedel, R. Mishra, A. Pelka, D. Kraus, B. Barbre, T. Döppner, and S. H. Glenzer, *Rev. Sci. Instrum.* **87**, 11E524 (2016).
- ⁵S. H. Glenzer and R. Redmer, *Rev. Mod. Phys.* **81**, 1625 (2009).
- ⁶K. Falk, C. L. Fryer, E. J. Gamboa, C. W. Greeff, H. M. Johns, D. W. Schmidt, M. Šmid, J. F. Benage, and D. S. Montgomery, *Plasma Phys. Controlled Fusion* **59**, 014050 (2016).
- ⁷G. Gregori, S. H. Glenzer, W. Rozmus, R. W. Lee, and O. L. Landen, *Phys. Rev. E* **67**, 026412 (2003).
- ⁸A. J. Visco, R. P. Drake, S. H. Glenzer, T. Döppner, G. Gregori, D. H. Froula, and M. J. Grosskopf, *Phys. Rev. Lett.* **108**, 145001 (2012).
- ⁹G. E. Ice and C. J. Sparks, *Nucl. Instrum. Methods Phys. Res., Sect. A* **291**, 110 (1990).
- ¹⁰H. Legall, H. Stiel, P.-V. Nickles, A. A. Bjeoumikhov, N. Langhoff, M. Haschke, V. A. Arkadiev, and R. Wedell, *Proc. SPIE* **5918**, 11–21 (2005).

- ¹¹U. Zastrau, C. R. D. Brown, T. Döppner, S. H. Glenzer, G. Gregori, H. J. Lee, H. Marschner, S. Toleikis, O. Wehrhan, and E. Förster, *J. Instrum.* **7**, P09015 (2012).
- ¹²E. J. Gamboa, D. S. Montgomery, I. M. Hall, and R. P. Drake, *J. Instrum.* **6**, P04004 (2011).
- ¹³E. J. Gamboa, C. M. Huntington, M. R. Trantham, P. A. Keiter, R. P. Drake, D. S. Montgomery, J. F. Benage, and S. A. Letzring, *Rev. Sci. Instrum.* **83**, 10E108 (2012).
- ¹⁴E. C. Harding, T. Ao, J. E. Bailey, G. Loisel, D. B. Sinars, M. Geissel, G. A. Rochau, and I. C. Smith, *Rev. Sci. Instrum.* **86**, 043504 (2015).
- ¹⁵U. Zastrau, E. J. Gamboa, D. Kraus, J. F. Benage, R. P. Drake, P. Efthimion, K. Falk, R. W. Falcone, L. B. Fletcher, E. Galtier, M. Gauthier, E. Granados, J. B. Hastings, P. Heimann, K. Hill, P. A. Keiter, J. Lu, M. J. MacDonald, D. S. Montgomery, B. Nagler, N. Pablant, A. Schropp, B. Tobias, D. O. Gericke, S. H. Glenzer, and H. J. Lee, *Appl. Phys. Lett.* **109**, 031108 (2016).
- ¹⁶U. Zastrau, K. Appel, C. Baetz, O. Baehr, L. Batchelor, A. Berghäuser, M. Banjafar, E. Brambrink, V. Cerantola, T. E. Cowan, H. Damker, S. Dietrich, S. Di Dio Cafiso, J. Dreyer, H.-O. Engel, T. Feldmann, S. Findeisen, M. Foes, D. Fulla-Marsa, S. Göde, M. Hassan, J. Hauser, T. Herrmannsdörfer, H. Höppner, J. Kaa, P. Kaever, K. Knöfel, Z. Konópková, A. Laso García, H.-P. Liermann, J. Mainberger, M. Makita, E.-C. Martens, E. E. McBride, D. Möller, M. Nakatsutsumi, A. Pelka, C. Plueckthun, C. Prescher, T. R. Preston, M. Röper, A. Schmidt, W. Seidel, J.-P. Schwinkendorf, M. O. Schoelmerich, U. Schramm, A. Schropp, C. Strohm, K. Sukharnikov, P. Talkovski, I. Thorpe, M. Toncian, T. Toncian, L. Wollenweber, S. Yamamoto, and T. Tschentscher, *J. Synchrotron Radiat.* **28**, 1393 (2021).
- ¹⁷T. R. Preston, S. Göde, J.-P. Schwinkendorf, K. Appel, E. Brambrink, V. Cerantola, H. Höppner, M. Makita, A. Pelka, C. Prescher, K. Sukharnikov, A. Schmidt, I. Thorpe, T. Toncian, A. Amouretti, D. Chekrygina, R. W. Falcone, K. Falk, L. B. Fletcher, E. Galtier, M. Harmand, N. J. Hartley, S. P. Hau-Riege, P. Heimann, L. G. Huang, O. S. Humphries, O. Karnbach, D. Kraus, H. J. Lee, B. Nagler, S. Ren, A. K. Schuster, M. Smid, K. Voigt, M. Zhang, and U. Zastrau, *J. Instrum.* **15**, P11033 (2020).
- ¹⁸U. Zastrau, A. Woldegeorgis, E. Förster, R. Loetsch, H. Marschner, and I. Uschmann, *J. Instrum.* **8**, P10006 (2013).
- ¹⁹H. H. Johann, *Z. Phys.* **69**, 185–206 (1931).
- ²⁰M. Smid, X. Pan, and K. Falk, *Comput. Phys. Commun.* **262**, 107811 (2021).
- ²¹M. S. del Rio and R. J. Dejes, *Proc. SPIE* **3152**, 148–157 (1997).
- ²²See <http://www.mvlz.com/ueditor/php/upload/file/20181116/154235404994-5020.pdf> for Princeton instruments: Pi-mte:2048b datasheet.
- ²³D. Roberts and M. Sulkanen, AXAF project science: Widths for characteristic x-ray lines, <https://wwwastro.msfc.nasa.gov/xraycal/linewidths.html>, 1997, accessed 10 July 2022.
- ²⁴H.-K. Chung, M. H. Chen, and R. W. Lee, *High Energy Density Phys.* **3**, 57 (2007).
- ²⁵G. Hölzer, M. Fritsch, M. Deutsch, J. Härtwig, and E. Förster, *Phys. Rev. A* **56**, 4554 (1997).